Excited-State Conformational/Electronic Responses of Saddle-Shaped *N,N′*-Disubstituted-Dihydrodibenzo[*a,c*]phenazines: Wide-Tuning Emission from Red to Deep Blue and White Light Combination

Zhiyun Zhang,[†,‡,§] Yu-Sin Wu,[‡,§] Kuo-Chun Tang,[‡] Chi-Lin Chen,[‡] Jr-Wei Ho,[‡] Jianhua Su,[†] He Tian,[*,†] and Pi-Tai Chou[*,‡]

[†]Key Laboratory for Advanced Materials and Institute of Fine Chemicals, East China University of Science & Technology, Shanghai 200237, P. R. China

[‡]Department of Chemistry, National Taiwan University, Taipei, 10617 Taiwan, R.O.C.

S *Supporting Information*

ABSTRACT: A tailored strategy is utilized to modify 5,10-dimethylphenazine (**DMP**) to donor−acceptor type *N,N′*-disubstituted-dihydrodibenzo[*a,c*]phenazines. The representative compounds **DMAC** (*N,N′*-dimethyl), **DPAC** (*N,N′*-diphenyl), and **FlPAC** (*N*-phenyl-*N′*-fluorenyl) reveal significant nonplanar distortions (i.e., a saddle shape) and remarkably large Stokes-shifted emission independent of the solvent polarity. For **DPAC** and **FlPAC** with higher steric hindrance on the *N,N′*-substituents, normal Stokes-shifted emission also appears, for which the peak wavelength reveals solvent-polarity dependence. These unique photophysical behaviors are rationalized by electronic configuration coupled conformation changes en route to the geometry planarization

in the excited state. This proposed mechanism is different from the symmetry rule imposed to explain the anomalously long-wavelength emission for **DMP** and is firmly supported by polarity-, viscosity-, and temperature-dependent steady-state and nanosecond time-resolved spectroscopy. Together with femtosecond early dynamics and computational simulation of the reaction energy surfaces, the results lead us to establish a sequential, three-step kinetics. Upon electronic excitation of *N,N′*-disubstituted-dihydrodibenzo[*a,c*]phenazines, intramolecular charge-transfer takes place, followed by the combination of polarization stabilization and skeletal motion toward the planarization, i.e., elongation of the *π*-delocalization over the benzo[*a,c*]phenazines moiety. Along the planarization, **DPAC** and **FlPAC** encounter steric hindrance raised by the *N,N′*-disubstitutes, resulting in a local minimum state, i.e., the intermediate. The combination of initial charge-transfer state, intermediate, and the final planarization state renders the full spectrum of interest and significance in their anomalous photophysics. Depending on rigidity, the *N,N′*-disubstituted-dihydrodibenzo[*a,c*]phenazines exhibit multiple emissions, which can be widely tuned from red to deep blue and even to white light generation upon optimization of the surrounding media.
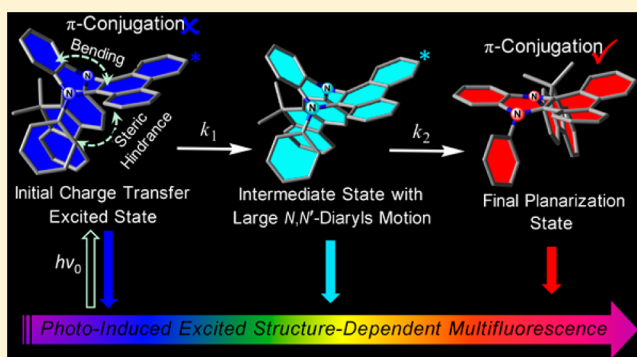
1. INTRODUCTION

Molecules having distinct differences in electronic configuration and/or structures between electronically ground and excited states may display very distinct photophysical properties, such as large Stokes-shifted and/or multiple emissions, which are of both fundamental and application interests.[1−7] A famous paradigm of the former case can be ascribed to the excited-state electron (charge) transfer such that a large change of dipole moment takes place between ground and lowest-lying excited states, inducing solvent dipolar relaxation for stabilization. As a result, the shift in emission spectra is a function of solvent polarity, dubbed solvatochromism.[2] The latter can be demonstrated in a number of cases, such as excited-state cis−trans isomerization,[3] ring opening/closure isomerization,[4]

proton-transfer tautomerism,[5] and geometry planarization,[6,7] resulting in a product that possesses a distinctly different structure from the ground state. As for the excited-state geometry planarization, the most typical case is twisted-to-planar,[6] which results from the rotation of the aryl rings around the C−C (or C−N) single bond as in the initially twisted biphenyls and biaryls.[6c,d] Another case, which is relatively rare, is the bent-to-planar[7] motion involving out-of-plane bending of a polycyclic aromatic molecule. Due to its scarcity, any new finding of bent-to-planar motion accompanied by unusual

photophysical properties may add a new chapter in this field to gain the associated fundamentals and applications.

Herein we report the photophysical studies of a series of N,N′-disubstituted-dihydrophenazines analogues exhibiting anomalous spectral properties. Owing to highly electron-rich and redox-active properties, dihydrophenazines have been widely investigated for application in organic electronics as p-type materials.[8,9] Meanwhile, the phenanthrene substitutes also serve as useful building blocks to develop novel optoelectronic architectures.[10] It is therefore demanding to develop new N,N′-disubstituted-dihydrophenazine derivatives comprising phenanthrene (as a fused ring) and to explore their associated physical and chemical properties from both fundamental and application perspectives. Upon pursuing hole-transporting and emissive materials based on arylamine-substituted phenanthrenes, in serendipity, we were very much attracted by an intriguing phenomenon from the relevant compound 9-(9,9-dimethyl-9H-fluoren-3-yl)-14-phenyl-9,14-dihydrodibenzo[a,c]phenazine (**FlPAC**, Scheme 1), which is colorless in solution yet exhibits

Scheme 1. Chemical Structures of N,N′-Disubstituted-Dihydrophenazine and Benzoannealated Analogues
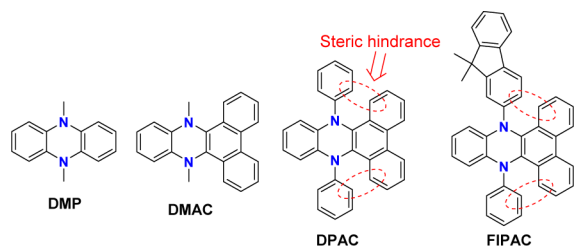

pronounced red emission. This emission peak wavelength is independent of solvent polarity with a Stokes shift, defined as the difference in energy between absorption and emission peaks, of >11,000 cm^{-1}.

We then performed a comprehensive literature search relevant to the photophysics of dihydrophenazines. In 1974, Huber and co-workers reported[11] the anomalous absorption and emission behavior of 5,10-dimethylphenazine (**DMP**, see Scheme 1), 5-methyl-10-phenylphenazine (**MPP**), and 5,10-diphenylphenazine (**DPP**). Exploiting symmetry analyses, they attributed the great Stokes shift to the energy gap between two different excited states, S_2 and S_1, responsible for the absorption and emission, respectively, since the $S_0 \rightarrow S_1$ transition is symmetrically forbidden and hence obscure in the absorption spectrum. Later, Schuster et al. reported[12] the absorption and emission behavior of benzoannealated analogues **DMP**, 9,14-dimethyl-9,14-dihydrodibenzo[a,c]phenazine (**DMAC**, Scheme 1) and 6,13-dimethyl-6,13-dihydrodibenzo[b,i]phenazine (**DMBI**), and imposed a similar symmetry rule-based explanation to rationalize the anomalous Stokes-shifted emission for **DMP** and **DMAC**. On the other hand, **DMBI** possesses symmetry-allowed $S_0 \rightarrow S_1$ transition and hence exhibits a normal Stokes-shifted emission.

If the mechanism discussed above were applicable to most dihydrophenazines and the derivatives, we would not have been puzzled by the enormously large Stokes-shifted emission in, e.g., **FlPAC**, for which the C_2 symmetry has been broken down. Interestingly, since Schuster's work and up to the current stage, no in-depth photophysical studies along with the excited-state dynamics of the N,N′-disubstituted-dihydrophenazines have been conducted, despite their vast usage in optoelectronic

applications.[8] We have thus strategically designed and synthesized a series of N,N′-disubstituted-dihydrophenazine and benzoannealated analogues (Scheme 1), in which the representative **DMAC**, **DPAC**, and **FlPAC** are the electron donor−acceptor type of dyads (vide infra). Structural analyses indicate that they all reveal significant nonplanar distortion of the dihydrodibenzo[a,c]phenazine framework as a result of steric hindrance between the N,N′-disubstitutes and phenanthrene ring (Figure 1). Remarkably, they all exhibit enormously
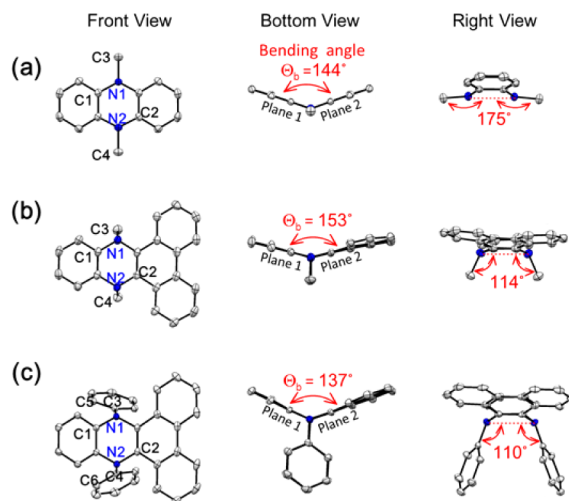
Figure 1. Single crystal structures of (a) **DMP**, (b) **DMAC**, and (c) **DPAC** and their three angles of view together with the selected angles. The bending angle between planes 1 (C1, N1, and N2) and 2 (N1, N2, and C2) is denoted as Θ_b for all titled compounds. Note that under this definition, a bending angle of 180° specifies the planarization between planes 1 and 2, while 0° indicates two parallel planes. Accordingly, from 0 to 180°, a larger bending angle indicates more planarization.

large Stokes-shifted emission. In this study, combining comprehensive solvent polarity and viscosity-dependent spectroscopy, time-resolved measurements, and computational approaches, we posit a generalized mechanism incorporating structural relaxation, namely a bent-to-planar transition of the V-shaped dihydrodibenzo[a,c]phenazine framework, to extend the π-conjugation. This, together with the significant charge-transfer character in the Franck−Condon excited state, accounts for the multiple emission behaviors of the titled N,N′-disubstitued-dihydrodibenzo[a,c]phenazines.

2. RESULTS AND DISCUSSION

2.1. Synthesis Strategy and Molecular Structure. N,N′-Dimethyl-dihydrophenazines **DMP** and **DMAC** were prepared by reduction-methylation of phenazine derivatives according to the standard literature procedure.[13] **DPAC** and **FlPAC** were prepared via a method of copper-promoted coupling starting from N^9,N^{10}-diphenylphenanthrene-9,10-diamine derivatives and aryl iodides (see Scheme S1 of the Supporting Information (SI)). Details of the synthetic route are elaborated in SI. All N,N′-disubstituted-dihydrophenazines were fully characterized with ^{1}H NMR, ^{13}C NMR, and high-resolution mass spectrometry (HRMS).

For the parent compound **DMP**, earlier theoretical calculation has pointed out the bent geometry (C_{2v}) of its molecular structure,[11] and later it has been further confirmed[8a] to have a single crystal structure, showing that the molecule is

bent along the N1−N2 axis and the intersecting planes of the two aryl rings along the N1−N2 axis form a bay with a bent angle Θ_b ($\angle C(1)-N(1)-N(2)-C(2)$ ~144°, see Figure 1). More specifically, the bent angle Θ_b is defined as the angle between two planes (of two opposite aryl rings) bisected and hinged by the two nitrogen atoms (see Figure 1). Furthermore, crystals of **DMAC** and **DPAC**[8h] were also obtained by slow evaporation of solvent from the dichloromethane/ethanol mixture solutions and examined by X-ray analysis. The three angles of view of these compounds' single crystal structures are shown in Figure 1, together with the selected angles. Derived from **DMP** with the addition of the nonlinear aromatic phenanthrene fused to dihydroquinoxaline, **DMAC** inherits the bent geometry, with a bent angle Θ_b at around 153°. The most pronounced difference among the geometry of these two crystal structures is the angle between the N1−C3 (N2−C4) and N1−N2 planes ($\angle C(3)-N(1)-N(2)$ and $\angle C(4)-N(2)-N(1)$, see Figure 1). The angle $\angle C(3)-N(1)-N(2)$ ($\angle C(4)-N(2)-N(1)$) of **DMP** is around 175°, while that of **DMAC** is reduced substantially to ~114°. Obviously, the difference mainly results from the steric hindrance between the substituted group on the N1 (N2) and phenanthrene ring (see Scheme 1 and Figure 1). On the other hand, **DPAC** and **FlPAC** are designed by replacing the N-methyl group of **DMAC** with aromatic rings. As shown in Figure 1c, compared with **DMAC**, **DPAC** exhibits higher nonplanar distortions (Θ_b ~137° and $\angle C(3)-N(1)-N(2)$ ($\angle C(4)-N(2)-N(1)$) ~110°) because of the bulkier substitutes and hence greater steric hindrance being imposed.

Upon electronic excitation of the above titled N,N'-disubstituted-dihydrodibenzo[a,c]phenazines, energetically favorable planarization takes place to elongate the π-conjugation. The bent-to-planar motion may encounter steric hindrance. This, together with the inherited excited-state charge-transfer property, results in novel and distinctive photophysical properties of these saddle-shaped molecules. Details are provided in the following sections.

2.2. Steady-State Emission Spectroscopy. The normalized absorption and emission spectra of **DMP**, **DMAC**, **DPAC**, and **FlPAC** in various solvents from nonpolar cyclohexane to polar acetonitrile are shown in Figure 2. The first absorption maximum of **DMP** is located at ~343 nm (in toluene), while the maxima of phenanthrene-fused derivatives (**DMAC**, **DPAC**, and **FlPAC**) are red-shifted by ~10 nm to that of **DMP**. The absorption onsets of **DPAC** and **FlPAC** are at about 400 nm. In sharp contrast, the onset of **DMAC**'s tails down to ~470 nm. This result affirms the above structural analyses of a more planar structure for **DMAC** (cf., **DPAC** and **FlPAC**) due to its smaller steric hindrance (see Figure 1), rendering a greater π-delocalization and hence lower energy gap.

All titled compounds, including **DMP**, exhibit a large Stokes-shifted emission. For **DMP**, the peak wavelength of fluorescence is located at 465 nm in, e.g., cyclohexane with a Stokes shift of ~8000 cm^{-1} (Figure 2a). For **DMAC**, **DPAC**, and **FlPAC**, shown in Figure 2b−d, respectively, the emission peak wavelength is even farther red-shifted, with the value of Stokes shift calculated to be >11,000 cm^{-1}. Importantly, the maximum of this anomalously long wavelength emission is nearly independent of solvent polarity, being red-shifted by <15 nm (537 cm^{-1}) from cyclohexane to acetonitrile for all titled compounds (Figure 2a−d).

In addition to the dominant large Stokes-shifted band maximized at ~610 nm, careful examination of **DPAC** and **FlPAC** also shows a weak but non-negligible normal Stokes-
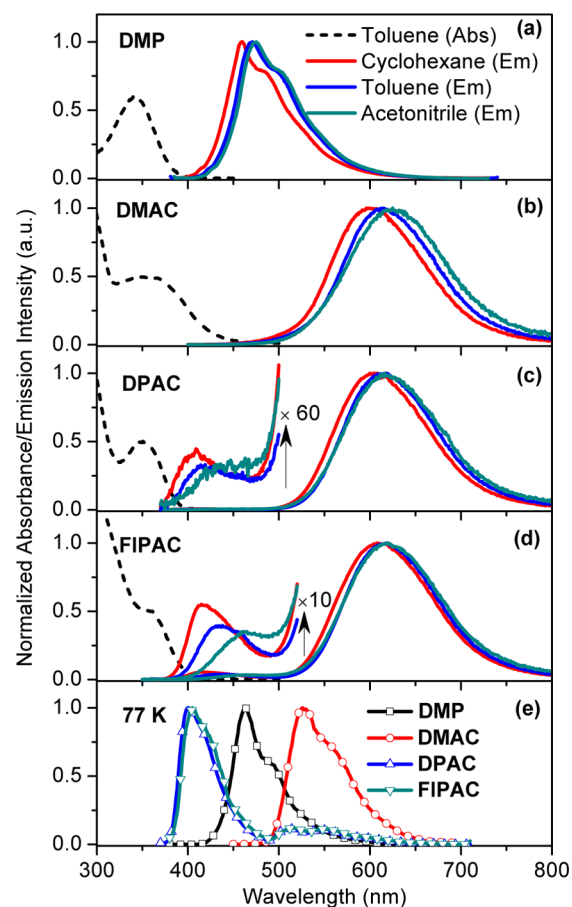
Figure 2. Steady-state absorption (in toluene, dashed line) and photoluminescence (solid line) spectra of (a) **DMP**, (b) **DMAC**, (c) **DPAC**, and (d) **FlPAC** in various solvents at room temperature, and (e) their photoluminescence spectra at 77 K in toluene glass. The enlarged blue emission profiles of **DPAC** and **FlPAC** are also shown in (c) and (d), respectively.

shifted band around the blue region. Both normal and large Stokes-shifted emissions share the same origin, i.e., the same Franck−Condon excited state, as evidenced by the identical excitation spectra, which are also overlapping with the absorption spectrum (Figure S1 for **FlPAC**). In stark contrast to the solvent-polarity insensitive 610 nm emission, the normal emission bands show substantial solvent polarity dependence, being red-shifted from cyclohexane to acetonitrile by 1800 and 2730 cm^{-1}, respectively, for **DPAC** and **FlPAC** (see enlarged area of Figure 2c,d).

We first pondered the mechanism of symmetry rule adopted for **DMP** (vide supra). However, the breakdown of C_2 symmetry in, e.g., **FlPAC**, makes the assignment of red emission originating from the symmetry restriction rule impossible. Also, the origin from solvatochromism has been eliminated because of the nearly solvent-polarity independence of the red emission (Figure 2). Alternatively and more plausibly, owing to the V-shaped nonplanar geometry of the titled compounds (Figure 1), we tentatively propose the occurrence of structural bending motion along the N(1)−N(2) axis for **DMAC**, **DPAC**, and **FlPAC** in the electronically excited state, reaching a planar configuration to a fully extended π-conjugation and hence an energy minimum.

The large-amplitude motion proposed above is expected to be viscosity dependent. To support this viewpoint, we first

investigated their emission property in the rigid toluene matrix at 77 K, in which the structural relaxation toward planarization is impeded. The results shown in Figure 2e at 77 K offer firm support; **DMAC**, **DPAC**, and **FlPAC** all exhibit solely normal Stokes-shifted emission at 525, 400, and 405 nm, respectively. Note that the additional emission bands of **DPAC** and **FlPAC** that appear in the range from 500 to 600 nm in the 77 K toluene solid matrix are assigned to the phosphorescence due to its >1 ms lifetime. In stark contrast, **DMP** still exhibits a large Stokes-shifted fluorescence at 470 nm in the 77 K toluene solid matrix, the spectral feature of which is nearly identical with that acquired at room temperature. Also, as shown in Figure S2, **DMAC**, **DPAC**, and **FlPAC** reveal normal Stokes-shifted emission in solid due to the lattice constraint, whereas a similar large Stokes-shifted emission is still observed in solid **DMP**. Unambiguously, the results lead us to conclude different origins of anomalous emission between **DMP** and its phenanthrene-fused derivatives **DMAC**, **DPAC**, and **FlPAC**. On the one hand, the anomalous long-wavelength emission for **DMP** has been reported to originate from the imposition of a symmetry rule (vide infra).[11] On the other hand, considering that the symmetry rule should not be temperature/viscosity dependent, the latter must involve a significant conformational change, plausibly toward planarization, in the excited state, such that the normal and anomalous Stokes-shifted emissions are tentatively ascribed to bent and planar forms, respectively.

The harnessing of the large amplitude internal motion can be elegantly demonstrated by using *n*-butanol as the media to fine-tune the ratiometric emission because its viscosity is relatively high (2.948 cP at 293 K, cf. 0.343 cP for CH_3CN at 298 K)[14] and is temperature sensitive,[15] suitable for probing the ratiometric changes of the emission in a steady state manner. Using **FlPAC** as a prototype, the decrease of temperature from 293 to 233 K is accompanied by the gradual increase of emission intensity in both red and blue regions (see Figure S3a). Because the associated peak wavelengths remain unchanged, the result may qualitatively be rationalized by a combination of slowing down the planarization process and the suppression of the nonradiative decay process. Further lowering the temperature from 233 to 173 K led to a decrease in intensity and slight blue shift of the red emission band from 610 to 595 nm, accompanied by an increase and broadening of the blue-green emission band (~450−520 nm) (Figure 3). As the temperature dropped toward 133 K, the red emission band disappeared; concomitantly, the sky blue-green emission band was shifted to shorter wavelengths and finally showed a blue emission maximized at 425 nm at 133 K. Also noteworthy is that the full width at half-maximum (fwhm) of the blue-green emission band was significantly reduced from 5802 cm^{-1} at 173 K to 3215 cm^{-1} at 133 K. Obviously, the temperature-dependent study of **FlPAC** in *n*-butanol revealed multiple band-like emissions covering the entire visible spectral range from red to deep blue. The changes in emission color can be viewed with the naked eye (inset of Figure 3) as well as by the color hue index of the Commission Internationale de L'Eclairage (CIE) coordinate (Figure S4). At 188 K, the CIE coordinate for **FlPAC** was calculated to be (0.33, 0.30), close to the coordinate (0.33, 0.33) of the standard white light illumination.

Temperature-dependent emission properties were also observed for **DPAC** and **DMAC** in *n*-butanol (see Figures S3 and S4). Nevertheless, there are discernible differences among these three compounds. For **DPAC**, shown in Figure S3b, the
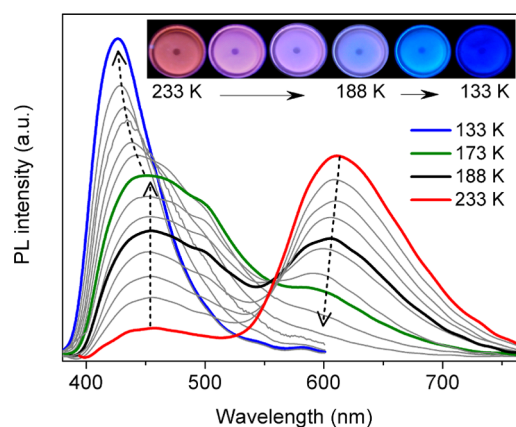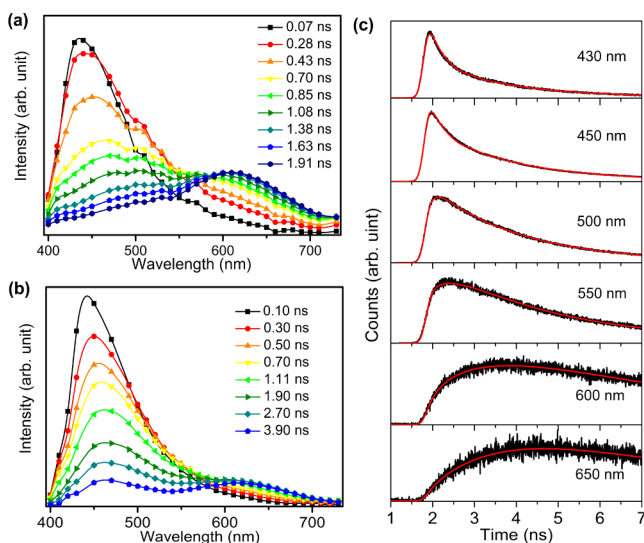

Figure 3. Temperature-dependent fluorescence spectra of **FlPAC** in *n*-butanol from 233 to 133 K with various viscosities. The arrows indicate the direction of fluorescence response upon reducing the temperature. Inset: represented photographs under 365 nm UV light.

decrease in intensity of the red emission band and hypsochromic shift of the blue-green emission took place at lower temperatures (~193 and ~163 K, respectively, cf. ~233 and ~173 K for **FlPAC**). As for **DMAC**, the emission intensity was continuously increased, accompanied by the hypsochromic shift from room temperature to 133 K. As a result, the emission was gradually tuned from red to green throughout the temperature-dependent study to 133 K (see Figures S3c and Figure S4 for the change in color index in the CIE coordinate).

The steady-state approach described above thus suggests that the planarization may couple with other electronic and/or structural relaxation processes to account for the observed multiple emissions that show various degrees of temperature dependence among **DMAC**, **DPAC**, and **FlPAC**. To shed light on the associated mechanism, we then further performed nanosecond time-resolved emission spectra and their corresponding dynamics in the viscous solvents, described below.

2.3. Nanosecond Time-Resolved Emission Spectroscopy. We realized that in a high-viscosity system, such as in the glycerol/ethanol (v/v 4:1) mixture with η ~171 cP[16] at 298 K, **DPAC** and **FlPAC** exhibited a much enhanced blue emission band versus the large Stokes-shifted red emission (see Figure S5), inferring the slowdown of the structure relaxation process, which makes feasible the time-resolved emission study at room temperature using the nanosecond time-correlated single-photon counting (TCSPC) technique. The corresponding relaxation dynamics can then be analyzed at each wavelength to reconstruct the temporal evolution of the emission spectrum. Accordingly, the spectral temporal evolutions of **DPAC** and **FlPAC** were recorded in a 4:1 glycerol/ethanol mixture at 298 K and are shown in Figure 4a,b, respectively. Upon Franck−Condon excitation, for the case of **FlPAC**, a deep-blue emission band maximized at around 435 nm promptly appeared (with a system response-limit rise of ~50 ps), which revealed a nice mirror image with respect to the absorption bands (see Figure 2d for the absorption). As the time elapsed, the short wavelength emission bands (~400−550 nm) were gradually decreased and red-shifted, whereas the long wavelength emission (~500−700 nm) continuously grew and reached its maximum intensity at ~610 nm. A similar temporal evolution pattern was observed in **DPAC** (see Figure 4a). It is interesting to note that the spectral temporal profiles of **DPAC** and **FlPAC** in glycerol/ethanol (v/v 4:1) at 298 K are similar to their

Figure 4. Reconstructed transient fluorescence of (a) **DPAC** and (b) **FlPAC** at different times in a 4:1 glycerol/ethanol mixture with viscosity of ~171 cP at room temperature by TCSPC at room temperature. (c) Fluorescence spectra decay traces recorded for **FlPAC** in the 4:1 glycerol/ethanol mixture at room temperature, of various wavelengths as depicted. See Table 1 for the fitting results.

temperature-/viscosity-dependent steady-state spectra in *n*-butanol (see Figures 3 and S3), reaffirming the involvement of large amplitude motion for the observed kinetics.

We then performed comprehensive spectral/dynamic analyses by plotting the rise and decay profiles at each crucial wavelength for **FlPAC**. The results are depicted in Figure 4c, while pertinent data are listed in Table 1. At the deep blue

Table 1. Fitting Results of TCSPC Spectroscopic Measurements for FlPAC in a 4:1 Glycerol/Ethanol Mixture at Room Temperature

λ_{probe} (nm)	population decay (ns)
430	τ_1: 0.35 (0.71), τ_2: 2.07 (0.29)
450	τ_1: 0.35 (0.53), τ_2: 2.00 (0.47)
500	τ_1: 0.35 (−1.00), τ_2: 0.35 (0.98), τ_3: 2.22 (0.02)
550	τ_1: 0.35 (−0.27), τ_2: 2.06 (0.04), τ_3: 4.58 (0.96)
600	τ_1: 0.35 (−0.19), τ_2: 2.06 (−0.70), τ_3: 4.58 (1.00)
650	τ_1: 2.06 (−0.92), τ_2: 4.83 (1.00)

region of 430 nm, the time-resolved fluorescence consists of two decay components of 0.35 and 2.07 ns (see Table 1). Upon monitoring at 500 nm, a rise time of 0.35 ns appears, as evidenced by a negative pre-exponential factor (see Table 1), which, within experimental error, correlates well with the 0.35 ns decay component detected at 430 nm. Although the emission at these two wavelengths reveals the same decay component of ~2 ns, the difference lies in that its contribution in intensity and hence population, monitored by the pre-exponential value (see Table 1), is substantially decreased at the bluer wavelength. This result indicates the spectral overlap of temporal evolution from 430 to 500 nm (Figure 4b). At the longest wavelength monitored at 650 nm, the overall kinetics can be well fitted by a rise (~2.06 ns) and a decay (~4.83 ns) component, in which the rise of ~2.06 ns matches exactly with the decay component (~2.06 ns) of the short wavelength at, e.g., 500 nm. The resolved 0.35, 2.0, and 4.8 ns time constants throughout the entire emission spectra, together with the

system-response-limited rise component at the very blue region (<430 nm), lead us to propose a sequential three-state reaction kinetics after electronic excitation, which incorporates the initially excited state, an intermediate state, and the final population state. The final population state possesses an energy minimized geometry that plausibly contains a planar-like dibenzo[*a,c*]phenazine moiety.

2.4. Femtosecond Fluorescence Up-Conversion and Relaxation Dynamics. As described above, the multiple emission bands and their corresponding relaxation dynamics in the nanosecond regime could be well resolved in the relatively high-viscous solvents, such as *n*-butanol and glycerol-ethanol mixture. Nevertheless, the retardation of motion imposed by the mechanical force (viscosity) makes the resolution of structural relaxation dynamics per se complicated. Moreover, in low-viscous solvents, as shown by the emission spectra of **DPAC** and **FlPAC** (see Figure 2c,d), despite the invariance of peak wavelength for the major red emission band, the minor blue emission band reveals a significant bathochromic shift upon increasing the solvent polarity from cyclohexane to acetonitrile, indicating that blue emission reveals a charge-transfer character in nature. Accordingly, in a low-viscous environment, solvent polarity and its associated relaxation may couple with structural relaxation, which then channel into the overall reaction dynamics. To shed light on the corresponding relaxation dynamics, we then carried out femto-picosecond time-resolved measurement by use of the fluorescence up-conversion technique. In this approach, **FlPAC** served as a prototype, and the study was carried out in toluene and acetonitrile to elucidate the comparative relaxation dynamics. As shown in Figure 5a and Table 2, in toluene, the relaxation
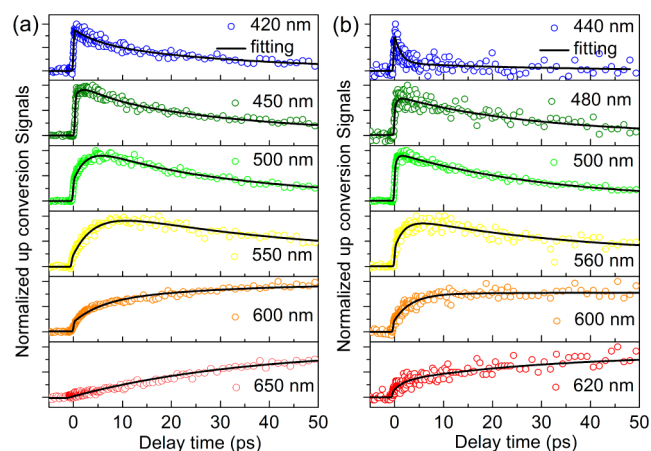
Figure 5. Femtosecond fluorescence transients (open circles) of **FlPAC** in aerated (a) toluene and (b) acetonitrile at room temperature observed at various wavelengths as depicted. The black solid lines denote the fitting curves. See Table 2 for the fitting results.

dynamics of emission at the blue side (420 nm) exhibited an instant rise (<120 fs), followed by a very fast and a fast decay component of ~5.6 and ~36 ps, respectively. Upon monitoring at 450 nm, a finite rise component (negative pre-exponential value) was fitted to be ~1.5 ps, accompanied by the 5.6 and 38 ps decay components. At 500 nm, the rise component increased its weighing ratio (increase of % in pre-exponential factor) and was lengthened to ~3.6 ps, accompanied by the decrease of the contribution from the 5.6 ps decay component. At 550 nm, the 5.6 ps decay component was not resolvable.

Table 2. Fitting Results of Femtosecond Fluorescence up-Conversion Measurement for FlPAC in Toluene and Acetonitrile[a]

relaxation time constants
In Toluene
420 nm [τ_1: 5.6 ps (0.34); τ_2: 36 ps (0.66)]
450 nm [τ_1: 1.5 ps (−0.47); τ_2: 5.6 ps (0.53); τ_3: 38 ps (0.47)]
500 nm [τ_1: 3.6 ps (−0.75); τ_2: 5.6 ps (0.32); τ_3: 38 ps (0.68)]
550 nm [τ_1: 4.5 ps (−0.98); τ_2: 38 ps (0.75); τ_p: 7.1 ns (0.25)]
600 nm [τ_1: 5.6 ps (−0.40); τ_2: 38 ps (−0.42); τ_p: 7.1 ns (1.00)]
650 nm [τ_1: 38 ps (−1.00); τ_p: 7.1 ns (1.00)]
In Acetonitrile
440 nm [τ_1: 1.8 ps (0.81); τ_2: 33 ps (0.19)]
480 nm [τ_1: 0.5 ps (−0.37); τ_2: 29 ps (1.00)]
500 nm [τ_1: 0.5 ps (−0.41); τ_2: 31 ps (1.00)]
560 nm [τ_1: 2.0 ps (−0.64); τ_2: 35 ps (0.77); τ_p: 4.3 ns (0.23)]
600 nm [τ_1: 3.4 ps (−0.73); τ_2: 33 ps (−0.05); τ_p: 4.3 ns (1.00)]
620 nm [τ_1: 2.0 ps (−0.30); τ_2: 33 ps (−0.58); τ_p: 4.3 ns (1.00)]

[a]The time constant τ_p of the population decay is determined from the TCSPC result and is used to the fitting of up-conversion signals.

Instead, in addition to the 38 ps decay component, a very long decay appeared, which could not be resolved but treated as a constant value, within the acquisition time window of ∼1000 ps. This long decay component was further resolved to be 7.1 ns by the TCSPC method (see Figure S6). Upon monitoring at 600 nm, the kinetic trace can be well fitted by two rise components of 5.6 and 38 ps and a population decay of 7.1 ns (see Figure 5a). Note that the rise times of 5.6 and 38 ps at 600 nm are the same as the 5.6 and 38 ps decay time constants monitored at 420 nm and <550 nm, respectively. Finally, at the very red emission region (650 nm), the fluorescence transient clearly exhibited only a rise component of 38 ps and a population decay of 7.1 ns. Similar kinetic patterns were obtained for **FlPAC** in acetonitrile (see Figure 5b and Table 2), except that the early fast decay component was decreased from 5.6 ps in toluene to ∼1.8−2.0 ps in acetonitrile; the other two time constants were measured to be ∼34 ps and 4.3 ns, which are slightly smaller than those of 38 ps and 7.1 ns obtained in toluene.

According to the above fluorescence up-conversion data, for simplicity, the overall structural relaxation process of **FlPAC** can be qualitatively described by a sequential kinetic pattern expressed as

$$R^* \xrightarrow{\tau_1} I^* \xrightarrow{\tau_2} P^* \qquad (1)$$

where R* specifies the initial excited state, I* is an intermediate with the local minimum energy, and P* denotes the final state with the global minimum energy along the structural relaxation process. R*, I*, and P* are all assumed to be the emissive states. In toluene, we reasonably assign the time constants of the R* → I* and I* → P* processes to be 5.6 ps (τ_1) and 38 ps (τ_2), respectively, followed by a population decay of the P* state of 7.1 ns. On this basis, the relatively complicated rise times of 1.5 ps (450 nm), 3.6 ps (500 nm), and 4.5 ps (550 nm) can thus be rationalized by the overlap between decay of R* and rise of I* species in this region; the cancellation of each other by different ratios of intensity results in shorting of the fitted rise time. Moreover, as for the R* emission of **FlPAC** in the blue, the steady-state spectrum (see Figure 2d) has revealed a charge-transfer property with a pronounced solvatochromism effect. Therefore, solvent relaxation should play a role, which

may channel into the overall reaction coordinates; in this case, the early relaxation dynamics is subject to polarization environments. This viewpoint is supported by the shorter time constant (τ_1) in toluene (5.6 ps) than in acetonitrile (1.8−2.0 ps).

Figure 6a depicts the reconstructed femto-picosecond spectral temporal evolution of **FlPAC** in acetonitrile. Several
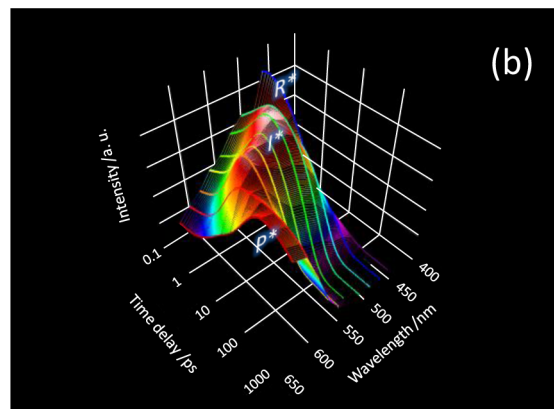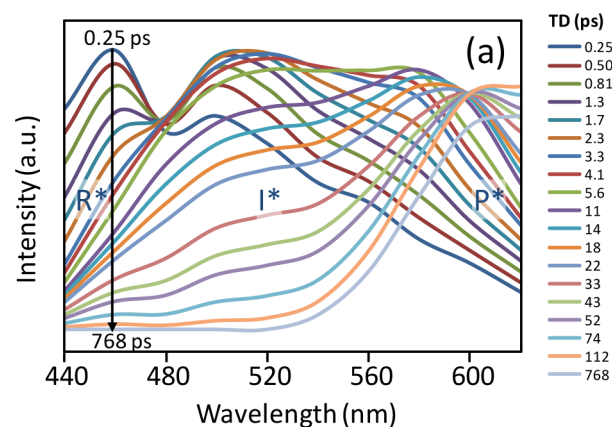

Figure 6. Reconstructed plots of **FlPAC** in acetonitrile at room temperature resolved by femtosecond fluorescence up-conversion: (a) spectral temporal evolution and (b) a 3-D surface plot, which provides a more intuitive way to perceive the temporal/spectral evolution and the excited state dynamics. Note that the time delay in (b) is in logarithm.

remarks can be pointed out from the layout of the spectra. First of all, the clearly resolved temporal emission region around 450−550 nm is obscure in the steady-state emission (cf. Figure 2d). Second, as the time elapsed, the overall spectrum reveals multiple bands as well as gradual bathochromic shift. The spectral peak quickly evolves from 460 nm (R*) to 520 nm (I*) within first ∼10 ps, and then finally the population emission band settles down at ∼610 nm (P*) after ∼40 ps. A similar trend of spectral temporal evolution was observed for **FlPAC** in toluene (see Figure S7), except that the spectral red shift is slower in the time domain than that in acetonitrile. Importantly, these femto-picosecond spectral temporal evolutions in low-viscous solvent exactly echo the nanosecond time-resolved data and temperature-/viscosity-dependent spectra in the high viscous solvents. The results manifest the occurrence of the structure evolution, which may also couple with the solvent relaxation at early dynamics, giving rise to the observed time-resolved multiple emission bands with complex kinetics. Figure 6b provides another angle of view to intuitively perceive

the excited-state dynamics of the proposed consecutive reaction mechanism (R* → I* → P*). Also, for clarity, various 3-D surface plots from other viewing angles are shown in Figure S8.

The femto-picosecond time-resolved measurements were also carried out for **DPAC** and **DMAC** (see Figures 7 and S9)
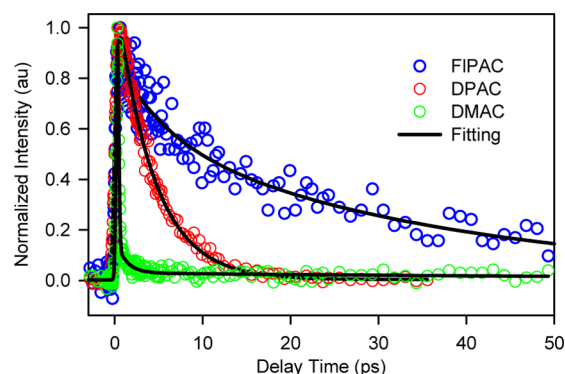
Figure 7. Femtosecond fluorescence transients of **FlPAC** (420 nm), **DPAC** (420 nm), and **DMAC** (440 nm) in aerated toluene.

to gain insights into the retardation of structural relaxation caused by the steric effect. Figure 7 shows the up-converted fluorescence transients of **DMAC**, **DPAC**, and **FlPAC** probed in the very blue region in toluene. The use of the same solvent rules out any discrepancy due to solvent viscosity or the polarity effect. The results, on the one hand, clearly indicate that the decay of **FlPAC** (5.6 ps, τ_1, see Table 2) is longer than that of **DPAC** (2.8 ps, τ_1, see Table S1), implying that the swing space of the bulky side chain, such as the fluorene derivatives in **FlPAC**, is more hindered than that of the phenyl derivative in **DPAC** during the structural relaxation. On the other hand, the system response limiting decay (<150 fs) in the blue region (440 nm) of **DMAC** implies its fast structural relaxation with negligible steric hindrance being imposed. Such a fast deactivation rate also well explains the lack of a blue emission band for **DMAC** in toluene (see Figure 2b).

2.5. Computational Approach. We then performed the computational approach in an aim to establish the associated mechanism, i.e., the excited-state conformational/electronic responses of these unique saddle-shaped compounds. In this study, we applied the time-dependent density functional theory (TD-DFT) approach (see Experimental Section) to access the

excited-state properties, in which the $S_0 \rightarrow S_1$ absorption is taken directly from the Franck–Condon excitation of the geometry optimized ground state, while the emission energy gap is calculated via the vertical $S_1 \rightarrow S_0$ transition from the structurally optimized S_1 state. The pertinent energy gaps of each calculated transition, together with experimental absorption and emission data in toluene, are listed in Table 3.

For these molecules, the results of calculation show that $S_0 \rightarrow S_1$ electronic transition corresponds to moving one electron from the highest occupied molecular orbital (HOMO) to the lowest unoccupied molecular orbital (LUMO) rather than some linear combination of orbitals[17] (see details in Table S2). As shown in Table 4, the electron density for both HOMO and LUMO of parent compound **DMP** is delocalized over the entire molecular framework. In sharp contrast, upon extending one of the phenylene-fused rings to phenanthrene in **DMP**, forming **DMAC**, **DPAC**, and **FlPAC**, due to the steric hindrance and structure nonplanarity, HOMO and LUMO, to certain degrees, are then localized at the central moiety N,N'-disubstituted-dihydropyrazine and the phenanthrene ring, respectively. For example, the HOMO of **DMAC** is mainly localized in the center moiety N,N'-dimethyl-dihydropyrazine and partially extended fusing rings (phenylene and phenanthrene) on the two sides. Replacing N,N'-dimethyl of **DMAC** with two bulky phenyls, forming **DPAC**, results in the further bending of two planes along the N1–N2 axis and hence the reduction of the π-conjugation, such that HOMO of **DPAC** is greatly localized in the center moiety N,N'-diphenyl-dihydropyrazine. Further replacing one N,N'-diphenyl of **DPAC** to fluoren-3-yl, forming **FlPAC**, the corresponding HOMO was then mainly localized in the N-fluoren-3-yl-dihydropyrazine moiety. On the other hand, LUMOs of **DMAC**, **DPAC**, and **FlPAC** are all mainly localized at the fused phenanthrene ring (see Table 4). The result of computation clearly demonstrates that the initial excited state for **DMAC**, **DPAC**, and **FlPAC**, in part, is associated with the charge-transfer character.

In the excited state, as unveiled by the fully optimized geometry, we learned that the molecular framework tends toward planarity from an initially prepared bending structure so that the two nitrogen lone pair electrons of the N,N'-phenazines participate in the elongation of π-conjugation and hence the stabilization, inducing a skeletal relaxation along Θ_b (Figure 1). For a full planar conformation ($\Theta_b \sim 180°$), the π-electron delocalization within the molecular framework can

Table 3. Experimental and Calculated Optical Characteristics for the Titled Compounds[a]

	Absorption $S_0 \rightarrow S_1$			Emission $S_1 \rightarrow S_0$			Stokes shift (cm^{-1})		Q.Y.	τ_f(ns)[c]
	λ_{exp}(nm)[b] (ε/M^{-1}cm^{-1})	λ_{calc}(nm)	f	λ_{exp}(nm)[b]	λ_{calc}(nm)	F	ΔE_{exp}[b]	ΔE_{calc}		
DMP	343 (13,600)	354	0.0001	473	471	0.0001	8013	7017	0.58	103 (84)[d]
DMAC	353 (6,100)	391	0.0779	612	603	0.0572	11989	8992	0.13	9.5
DPAC	347 (9,600)	387	0.1079	423	460	0.1676	5177	4100	0.001	<50 ps [450nm]
				613	564	0.1295	12505	8109	0.22	11.6 [650nm]
FlPAC	361 (19,600)	401	0.1473	433	493	0.1521	4606	4654	0.005	<50 ps [450nm]
				618	567	0.1614	11520	7301	0.17	11.0 [650nm]

[a]Data were recorded in degassed toluene at room temperature; see details in SI for fluorescence quenching in aerated toluene. λ_{exp} = experimental lowest-lying absorption or emission wavelengths, λ_{calc} = calculated lowest-lying absorption or emission wavelengths, ε = molar extinction coefficient, f = oscillator strengths, ΔE_{exp} = experimental Stokes shift, ΔE_{calc} = calculated Stokes shift, Q.Y. = emission, quantum yield, τ_f = population decay time. [b]The experimental values are taken from the peak wavelength of the absorption and emission. [c]The population decay time constants, which are measured by TCSPC (Edinburgh FL 900). [d]Reference12, determined in argon purged benzene at room temperature.

Table 4. Frontier Molecular Orbital Contours of the Titled Compounds in Optimized Ground-State Geometries[a]

	DMP	DMAC	DPAC	FlPAC		
Bending Angle (Θ_b)	146°	151°	138°	136°	133°	160°
LUMO						
HOMO						

[a] Also shown are FlPAC with relaxed structures in the S_1 excited state at the local (133°) and global (160°) minima.

thus be greatly extended. We then performed potential energy surface (PES) simulation scanning along the bending angle Θ_b for all phenanthrene-fused molecules from 100 to 180° in both S_0 and S_1 states. Clearly, in the lowest-lying electronically excited state, the structural relaxation toward planarization is thermodynamically favorable for all phenanthrene-fused compounds. We also realize, however, that amid the change of Θ_b toward a global minimum energy, the planarization process also induces the steric effect of the hinged N,N'-disubstitutes; hence, their concomitant structural relaxation is necessary, which makes possible the existence of an intermediate state with local minimum energy described below.

Using **FlPAC** as a paradigm, Figure 8 depicts the simulated PES for **FlPAC** scanning along Θ_b for both ground and lowest
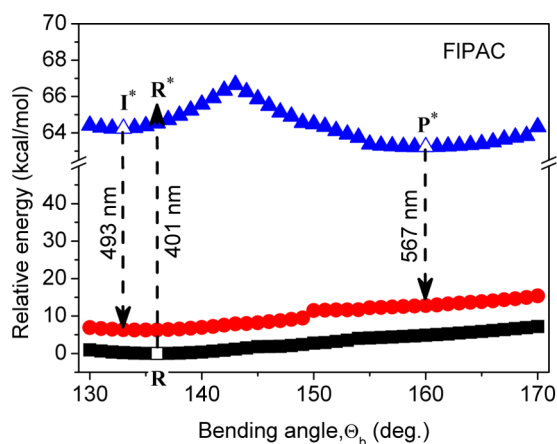
Figure 8. Calculated PES scanned along the change of bending angles Θ_b from 130 to 170° in an increment of 1° for **FlPAC** in the first excited state (S_1(blue ▲)), and ground state, in which S_0(red ●) denotes the vertical transition from S_1(blue ▲) in a specific Θ_b. S_0(black ■) is a ground-state optimized state at the same Θ_b. Open data symbols black □ and blue △ mark the global (or local) minimum of the PES for S_0(black ■) and S_1(blue ▲), respectively. Note: R* denotes the initial prepared S_1 state, from which only structural relaxation along Θ_b to the intermediate I* (see text) is depicted. For simplicity, other relaxation processes, such as vibrational deactivation and solvent relaxation processes, are omitted. More explicit depiction and delineation of the corresponding relaxation pathways can be found in Figure 10.

excited states, for which the geometry has been fully optimized at each value of Θ_b. As a result, at the ground state, the Θ_b value for the geometry optimized structure is 136°. We denote this geometry optimized ground state as R. The vertical electronic transition of the R state is calculated to be 401 nm (see Table 3), which is denoted as the Franck−Condon excited state R* (also defined in eq 1). Scanning Θ_b along the S_1 PES, the global minimum was located at Θ_b = 160° and is represented by P*. Importantly, in addition to the global minimum along Θ_b in the S_1 state, **FlPAC** was found to have a local minimum at Θ_b = 133°, denoted as I*, along the structural relaxation pathway (see Figure 8). The vertical transition from these two excited-state minima, i.e., I* → I and P* → P, is calculated to be 493 and 567 nm, respectively. On the one hand, the estimated 401 nm excitation and 493 nm emission for **FlPAC** correlates well with the steady-state ∼420−550 nm emission resolved from the temperature-dependent study in *n*-butanol (Figure 3) as well as nanosecond (Figure 4b) and femto-picosecond (Figure 6) time-resolved spectra. On the other hand, the calculated 567 nm emission wavelength matches the onset of the large Stokes-shifted red emission (λ_{max} ∼610 nm) measured in all solvents applied in this study.

Further detailed frontier analyses (see Table 4) also indicate that the R* state prepared from the vertical excitation can be ascribed to a HOMO → LUMO transition with an obvious charge-transfer character from the N-fluoren-3-yl-N,N'-dihydropyrazine moiety (donor) to the phenanthrene-fused ring (acceptor). This viewpoint is also supported by the calculated dipole moment of 15.24 D in R*, which is significantly larger than that (2.33 D) of the S_0 state. Moreover, as shown by its rather localized frontier orbitals, i.e., electron density distribution in N-fluoren-3-yl-N,N'-dihydropyrazine and phenanthrene-fused ring for HOMO and LUMO, respectively (see Table 4), the charge-transfer property of the I* state is apparent, the dipole moment of which is calculated to be as large as 17.84 D. On the other hand, for the P* state, due to the planarization of the phenazine chromophore, the extensive π-electron delocalization significantly reduces the ππ* energy gap, which leads to the dispersal of the local charge-transfer character. This is evidenced by the drastically different contribution of the frontier orbitals (HOMO/LUMO) for **FlPAC** in P*, in which the population of electron density is spread over the entire π-framework of the phenanzine-fused

ring rather than localized at the N-fluoren-3-yl side chain as in the case of R* (136°) and I* (133°). Additional support is the relatively small dipole moment calculated for P* (6.74 D) and the nearly solvent polarity independence of the P* emission peak wavelength (Figure 2d), despite its anomalously large Stokes shift.

As for **DPAC**, the PES simulation scanning along Θ_b (Figure S10) in the S_1 state also resulted in a local minimum I* at $\Theta_b = 134°$ and a global minimum P* at $\Theta_b = 161°$. For I*, the corresponding localized frontier orbitals for HOMO (at N,N'-diphenyl-dihydropyrazine) and LUMO (at phenanthrene-fused ring, Table S3), together with the calculated large dipole moment ($\sim$12.40 D), also led to the conclusion of its charge-transfer property. The charge-transfer character is also apparent from the vertical excitation of the geometry optimized ground state (R*, $\Theta_b = 138°$). The smaller dipole moment of R* for **DPAC** (12.34 D, cf. **FlPAC** (15.24 D)) may qualitatively be rationalized by the weaker electron-donating ability of benzene (**DPAC**) than fluorene in **FlPAC**. The global minimum P* ($\Theta_b = 161°$) of **DPAC** also possesses a planar phenanthrene moiety that extends the $\pi\pi^*$ (HOMO/LUMO) configuration (see Table S3 for frontier orbital analysis) with a smaller dipole moment (7.80 D).

In addition to the difference in Θ_b among R*, I*, and P*, also noted is the changes of space/orientation on the N,N'-disubstituted side chain among the three states. For example, from the R* state at $\Theta_b = 136°$ to the local minimum I* at $\Theta_b = 133°$, the results of calculation for **FlPAC**, shown in Figure 9,
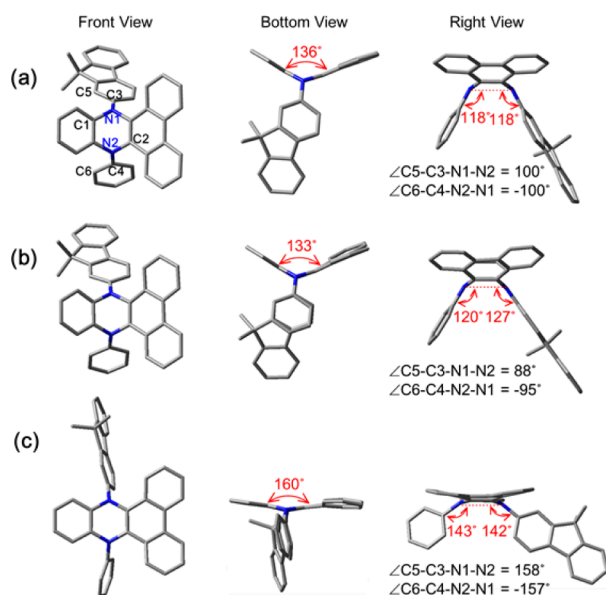

Figure 9. DFT optimized geometry of **FlPAC** (a) in the S_0 ground state at the global minimum ($\Theta_b = 136°$), (b) in the S_1 excited state at the local minimum ($\Theta_b = 133°$), and (c) in the S_1 excited state at the global minimum ($\Theta_b = 160°$), and three views together with the selected angles.

indicate the conformational change at the N,N'-diaryls site via swinging and rotating round their jointed nitrogen atoms, i.e., an increase of $\angle$C3–N1–N2 from 118° to 127° and a decrease of $\angle$C5–C3–N1–N2 from 100° to 88°. The results indicate that **FlPAC**, along the planarization, may encounter steric hindrance raised by the N,N'-disubstituted side chain. Thus, the dynamics of structural relaxation should be affected by the

N,N'-disubstituted side chain motion, which is slowed down upon increases in the bulky side chain with more steric hindrance (Scheme 1 and Figure 1). Qualitatively, this viewpoint could be supported by the computational approach. Upon scanning Θ_b along the planarization (I* → P*), internal energy barriers of 2.0 kcal/mol ($\Theta_b \sim 144°$) and 0.7 kcal/mol ($\Theta_b \sim 141°$) were calculated for **FlPAC** and **DPAC**, respectively, while virtually no barrier could be resolved for **DMAC** (see PES in Figure S10). The results are consistent with the increasing bulkiness of the side-chain in the order of **DMAC** < **DPAC** < **FlPAC**. Meanwhile, the level/functional of current computation did not allow us to identify any barriers along the R* → I* process. Experimentally, however, the retardation of structural relaxation caused by the steric effect was observed with the same trend (see Figure 7, vide supra).

2.6. Discussion. In this study, we have performed comprehensive studies on steady-state polarity, viscosity, and temperature-dependent spectroscopy, nanosecond to femto-second time-resolved spectroscopy, and dynamics in various viscosity and polarity environments. Together with the computational approach elaborated in the above section, we are now able to propose a three-step kinetics mechanism using **FlPAC** as a paradigm. Starting from excitation of the global minimum S_0 ($\Theta_b = 136°$) in the ground state, Figure 10 only
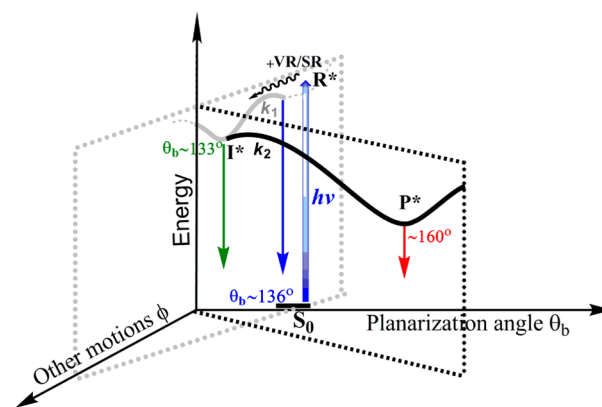
Figure 10. Proposed structural relaxation mechanism of **FlPAC** in the first electronically excited states along the skeletal motions in toluene. VR: vibrational relaxation, SR: solvent relaxation. Limited by the 3-D plot, it is not possible to draw the solvent polarization coordinate. The SR process is only depicted by a decrease in energy using a zigzag arrow symbol.

depicts internal structural relaxation in the S_1 state, in which the PES along the planarization angle Θ_b is singled out, while the rest of the coordinates relevant to structural motions are simply summed up and denoted as ϕ. The mechanical force resulting from viscosity and solvent polarity effects, which may affect the corresponding relaxation dynamics, are not shown in this plot. Also, limited by the 3-D plot, it is not possible to draw the solvent polarization coordinate in Figure 10, so internal conversion (the vibrational relaxation, VR) and solvent relaxation (SR) are simply combined in the initial structural relaxation and depicted by use of a zigzag arrow symbol.

Upon vertical excitation of **FlPAC** ($\Theta_b = 136°$), intra-molecular charge transfer takes place simultaneously from the N,N'-disubstituted chromophore to the phenazine moiety, denoted by a charge-transfer state R* (see Figure 10). The vibrationally hot and unfavorable polarization configuration is subsequently subject to a rapid internal conversion and solvent

relaxation, the time scale of which may couple with the small structural relaxation in the low-viscous environment, reaching a structurally relaxed local minimum I*. Note that amid the R* → I* process, despite the small variation of Θ_b, prominent conformational change takes place at the N,N'-diaryls side chains, which swing and rotate round their jointed nitrogen atoms (coordinate ϕ in Figure 10). Subsequently, driven by the thermodynamically favorable π-delocalization over the benzo-[a,c]phenazine moiety, I* → P* planarization takes place. Along the planarization, **FlPAC** (and **DPAC**) encounters steric hindrance raised by the N,N'-disubstituted side chain, resulting in a barrier at Θ_b ~144° (~141° for **DPAC**). The combination of initial charge-transfer state, intermediate, and the final planarization state renders the full spectrum to account for their anomalous emission and the associated kinetics. Using a simplified sequential kinetic model R* → I* → P*, in low viscous solvents, the rates of structure relaxation of R* and I* are measured to be fast, 2−6 and 33−38 ps, respectively, in toluene or acetonitrile. Their associated steady-state emission intensity is thus rather weak, for which the I* emission is hindered under the intense P* population emission (see Figure 2d) but has been resolved in the highly viscous solvents as well as by the femtosecond fluorescence up-conversion experiment in toluene and acetonitrile.

Finally, among the titled compounds investigated, we have to point out the perhaps exceptional case, **DMP**, according to previous report.[11,12] In our computational approach, the S$_0$ → S$_1$ (354 nm) transition for **DMP** is optically inaccessible ($^1A_1$ → $^1A_2$ in the C_2 point group) with an oscillator strength (f) of ~0.0001, and the calculated S$_0$ → S$_2$ (327 nm) transition is allowed with an f of ~0.4436. Similar result was obtained by Huber and co-workers[11] using a semi-empirical approach. Experimentally, the molar extinction coefficient (ε) of the absorption band at 343 nm is measured to be 13,600 M^{-1} cm^{-1}, which can be assigned to the allowed S$_0$ → S$_2$ transition. Therefore, the calculated S$_0$ → S$_1$ (354 nm) forbidden transition does not seem to be sufficiently low in energy to account for the large Stokes-shifted emission peak wavelength at 473 nm. Previously, it was not possible for Huber and co-workers to calculate the geometry relaxed S$_1$ → S$_0$ emission. To gain an in-depth insight into the origin of the anomalous Stokes shift of **DMP** emission, we have performed geometry optimization for both the ground and the excited (emitting) states. As a result, Θ_b values for the most stable ground/excited states (S$_0$/S$_1$) are calculated to be 146°/170° for **DMP**. Furthermore, for **DMP** the vertical (Franck−Condon) S$_1$ → S$_0$ emission from the structurally relaxed excited state is calculated to be 471 nm (see Table 3), which matches the observed 473 nm emission. If so, after excitation, **DMP** also shows prominent structural change (146° → 170°), stabilization energy, and hence Stokes-shifted emission. However, similar to Huber[11] and Schuster's[12] cryogenic experiments, we also observed a large Stokes-shifted ~470 nm fluorescence for **DMP** in the 77 K toluene solid matrix (vide supra), which is quite different from all other titled compounds that exhibit normal emission in the 77 K toluene solid matrix.

For a small molecule like **DMP**, we then wondered if the prominent structural change (146° → 170°) could take place in the excited state in the 77 K rigid toluene solid matrix. In this regard, Wan and co-workers have reported a nonplanar compound dibenz[b,f]oxepin with a large Stokes-shifted emission both in solution and rigid conditions.[7a] They thus proposed a change from a nonplanar ground state to a more

planar fluorescent excited singlet state for rationalization. Meanwhile, they considered that the torsional motion might have a very low activation barrier for dibenz[b,f]oxepin at 77 K in a 2-propanol/ether glass. This explanation may be applicable to **DMP**. However, more direct and convincing evidence is needed to prove that large amplitude motion during planarization can still take place for **DMP** in the 77 K rigid matrix. Support of this viewpoint unfortunately is still pending. Nevertheless, it is evident that the symmetry rule imposed previously by Huber and co-workers should explain, in part, the observed large Stokes-shifted emission for **DMP**.

It is also worthwhile to note that Schuster et al.[12] also studied **DMAC** and observed large Stokes-shifted emission (~600 nm in benzene). Similar to **DMP**, they invoked the symmetry forbidden S$_0$ → S$_1$ transition for rationalization. In this study, our TD-DFT calculation gives an S$_0$ → S$_1$ oscillator strength of 0.07 (Table 3), which is considered to be a partially allowed transition. In addition, the emission spectrum at ~520 nm of **DMAC** in the 77 K toluene solid matrix is much blue-shifted with respect to its room temperature emission (~610 nm, see Figure 2e). Considering that the symmetry rule should not be temperature/viscosity dependent, the imposition of forbidden transition is not sufficient for rationalizing the large Stokes-shifted emission of **DMAC**. Therefore, a significant conformational change, i.e., the planarization of the benzo[a,c]-phenazines moiety, should also take place in the excited state for **DMAC** (vide supra).

3. CONCLUSION

In summary, we report on the unusual photophysical behavior and comprehensive investigation of a series of saddle-shaped N,N'-disubstituted-dihydrodibenzo[a,c]phenazine donor−acceptor dyads (**DMAC**, **DPAC**, and **FlPAC**), derived from 5,10-dimethylphenazine (**DMP**) by extending one of the phenylene-fused rings to phenanthrene. Anomalously large Stokes-shifted emission (up to ~12,000 cm^{-1}), with slightly solvent polarity dependence, has been observed for all compounds; additionally, a weak normal Stokes-shifted band with an obvious solvatochromic effect has been found for the N,N'-diaryl-dihydrodibenzo[a,c]phenazines (**DPAC** and **FlPAC**). While all of the compounds, but **DMP**, exhibit prominent normal Stokes-shifted emission in rigid environments, the interpretation based on the symmetry selection rule[11] must be toned down. Instead, combining comprehensive spectroscopy, time-resolved measurements, and computational approaches, we conclude that the multifluorescence occurs from a sequential three-state electronic/structural relaxation process described above. As depicted in Figure 10, the interplay among solvatochromism at the early relaxation stage, the structural planarization, i.e., elongation of π-conjugation, accompanied by the side chain relaxation, and hence the possible steric hindrance, harnesses the emission properties. As a result, depending on the surrounding environment, a wide-tuning emission color from red to deep blue or even to white light generation can be achieved. These unusual and unique characters make feasible the titled phenazines and their future analogues for probing environment rigidity or local viscosity or even for the fabrication of light devices, wherein host materials such as polymers can be intentionally rather soft so that decent viscosity can be attained for ratiometric tuning of the multiple emission bands (for example, see Figure S14). The associated geometry relaxed phenomena of these titled phenazines thus provide a new paradigm en route to versatile lighting materials.

EXPERIMENTAL SECTION

Synthesis and Characterization. All reagents and solvents were purchased from commercial sources and were of analytical grade. Details of the synthetic procedures are provided in SI as well as compound characterization.

^1H and ^{13}C NMR spectra were recorded on a Bruker AM 400 spectrometer, operating at 400 and 100 MHz, respectively. HRMS spectra were recorded with a Waters electrospray ionization mass spectroscope. The intensity data of X-ray diffraction were collected on a Rigaku RAXIS RAPID IP imaging plate system with MoKα radiation (λ = 0.71073 Å).

Spectroscopic Measurements. Steady-state absorption and emission spectra were recorded by a Hitachi (U-3310) spectrophotometer and an Edinburgh (FS920) fluorimeter, respectively, but temperature-dependent fluorescence measurements of the samples, from 293 to 133 K in *n*-butanol, were collected by an optical assembly at the entrance slit of a polychromator (blazed at 150 nm) coupled with a sensitive image charge coupled detector (ICCD, Princeton Instruments, PI-MAX3). A Linkam FTIR 600 liquid-nitrogen cooling stage was employed to hold the sample and control the temperature.

Detailed time-resolved spectroscopic measurements have been reported previously elsewhere.[18] In brief, nanosecond time-resolved studies were performed with an Edinburgh FL 900 TCSPC system with a pulsed hydrogen- or nitrogen-filled lamp as the excitation light source. Data were fitted with sum of exponential functions using the nonlinear least-squares procedure in combination with the convolution method.

Ultrafast spectroscopic studies were performed with a femtosecond fluorescence up-conversion system (FOG100, CDP) pumped by the same femtosecond oscillator (Tsunami, Spectra-Physics) with a central output wavelength at 760 nm. In this measurement, fluorescence from a rotating sample cell, following the excitation at 380 nm (SHG of 760 nm), was collected, focused, and frequency summed in a BBO crystal, along with an interrogation gate pulse at a designated delay time with respect to the pump pulse. A $\lambda/2$ waveplate was used to set the pump polarization at the magic angle (54.7°) with respect to gate pulse for preventing the fluorescence anisotropy contributed by solute reorientation. Fluorescence up-conversion data were fitted to the sum of exponential functions convoluted with the instrument response function (IRF). The IRF was determined from the Raman scattering signal, and its profile was fitted to a Gaussian function with fwhm of ~150 fs.

The solvent used in this study was spectral grade and was used upon receipt (from Merck Inc.) without further purification. The degassed solvent was obtained by three freeze−pump−thaw cycles.

Time-Resolved Emission Spectra (TRES).[19] TRES are constructed in way that we started with measurement of the time-resolved decays at a number of designated wavelengths across the emission spectrum, $I(\lambda,t)$. The intensity decays are wavelength dependent. In order to calculate the TRES one computes a new set of intensity decays, which are normalized so that the time integrated intensity at each wavelength is equal to the steady-state intensity at that wavelength. This is done by the following equation

$$H(\lambda) = \frac{F(\lambda)}{\int_0^\infty I(\lambda, t)dt}$$

where $F(\lambda)$ is the steady-state emission spectrum, and $H(\lambda)$ is the volume, which when multiplied by the time-integrated intensity at the same wavelength is equal to the steady-state intensity at that wavelength. Accordingly, the normalized intensity decay functions can be expressed as $I'(\lambda,t) = H(\lambda)I(\lambda,t)$, which can be used to calculate the intensity at any wavelength and time to construct actual TRES.

Computational Methodology. For all title molecules, the geometries of the ground state were optimized by the DFT method, and excited state structures with related photophysical properties were calculated by the TD-DFT method with B3LYP hybrid function in combination with polarizable continuum model. The 6-31+G(d,p) basis set was employed for all atoms. In addition, for better understanding the molecular conformational changes in-between the electronically ground and first excited states, potential energy surfaces (PES) for the first excited state and ground state of all title molecules were computed and scanned along the bending angle, which was defined between plane 1 (C1, N1, and N2) and plane 2 (N1, N2, and C2) as a constraint (see Figure 1). We progressively scanned the bending angle spanning from 100 to 180° for every 10 °, and applied finer scanning steps per degree between 130−170°. All theoretical calculations were performed using the Gaussian 09 program.[20]

ASSOCIATED CONTENT

⑤ Supporting Information

Additional crystallographic (including CIF), computational, and spectroscopic data along with complete ref 20 are provided. The Supporting Information is available free of charge on the ACS Publications website at DOI: 10.1021/jacs.5b03491.

AUTHOR INFORMATION

Corresponding Authors
*tianhe@ecust.edu.cn
*chop@ntu.edu.tw

Author Contributions
§These authors contributed equally.

Notes
The authors declare no competing financial interest.

REFERENCES

(1) (a) Doroshenko, A. O. *Theor. Exp. Chem.* **2002**, *38*, 135−155. (b) Vollmer, F.; Rettig, W.; Birckner, E. *J. Fluoresc.* **1994**, *4*, 65−69.

(2) (a) Chien, Y.-Y.; Wong, K.-T.; Chou, P.-T.; Cheng, Y.-M. *Chem. Commun.* **2002**, 2874−2875. (b) Wong, K.-T.; Ku, S.-Y.; Cheng, Y.-M.; Lin, X.-Y.; Hung, Y.-Y.; Pu, S.-C.; Chou, P.-T.; Lee, G.-H.; Peng, S.-M. *J. Org. Chem.* **2005**, *71*, 456−465. (c) Terenziani, F.; Painelli, A.; Katan, C.; Charlot, M.; Blanchard-Desce, M. *J. Am. Chem. Soc.* **2006**, *128*, 15742−15755. (d) Marini, A.; Muñoz-Losa, A.; Biancardi, A.; Mennucci, B. *J. Phys. Chem. B* **2010**, *114*, 17128−17135. (e) Liu, C.; Tang, K.-C.; Zhang, H.; Pan, H.-A.; Hua, J.; Li, B.; Chou, P.-T. *J. Phys. Chem. A* **2012**, *116*, 12339−12348.

(3) (a) Sension, R. J.; Repinec, S. T.; Szarka, A. Z.; Hochstrasser, R. M. *J. Chem. Phys.* **1993**, *98*, 6291−6315. (b) Gepshtein, R.; Leiderman, P.; Huppert, D.; Project, E.; Nachliel, E.; Gutman, M. *J. Phys. Chem. B* **2006**, *110*, 26354−26364. (c) Stavrov, S. S.; Solntsev, K. M.; Tolbert, L. M.; Huppert, D. *J. Am. Chem. Soc.* **2006**, *128*, 1540−1546. (d) Gil, M.; Waluk, J. *J. Am. Chem. Soc.* **2007**, *129*, 1335−1341. (e) Zhu, L.; Li, X.; Zhang, Q.; Ma, X.; Li, M.; Zhang, H.; Luo, Z.; Ågren, H.; Zhao, Y. *J. Am. Chem. Soc.* **2013**, *135*, 5175−5182.

(4) (a) Pullen, S. H.; Anderson, N. A.; Walker, L. A.; Sension, R. J. *J. Chem. Phys.* **1998**, *108*, 556−563. (b) Tang, K.-C.; Rury, A.; Orozco, M. B.; Egendorf, J.; Spears, K. G.; Sension, R. J. *J. Chem. Phys.* **2011**, *134*, 104503. (c) Kim, S.; Yoon, S.-J.; Park, S. Y. *J. Am. Chem. Soc.* **2012**, *134*, 12091−12097.

(5) (a) Waluk, J. *Conformational Analysis of Molecules in Excited States*; Wiley-VCH: New York, 2000. (b) Tanner, C.; Manca, C.; Leutwyler, S. *Science* **2003**, *302*, 1736−1739. (c) Huynh, M. H. V.; Meyer, T. J. *Chem. Rev.* **2007**, *107*, 5004−5064. (d) Fang, C.; Frontiera, R. R.; Tran, R.; Mathies, R. A. *Nature* **2009**, *462*, 200−204. (e) Hsieh, C.-C.; Jiang, C.-M.; Chou, P.-T. *Acc. Chem. Res.* **2010**, *43*, 1364−1374. (f) Hsieh, C.-C.; Chou, P.-T.; Shih, C.-W.; Chuang, W.-T.; Chung, M.-W.; Lee, J.; Joo, T. *J. Am. Chem. Soc.* **2011**, *133*, 2932−2943. (g) Demchenko, A. P.; Tang, K.-C.; Chou, P.-T. *Chem. Soc. Rev.* **2013**, *42*, 1379−1408.

(6) (a) Valat, P.; Wintgens, V.; Kossanyi, J.; Biczok, L.; Demeter, A.; Berces, T. *J. Am. Chem. Soc.* **1992**, *114*, 946−953. (b) Demeter, A.; Bérces, T.; Biczók, L.; Wintgens, V.; Valat, P.; Kossanyi, J. *J. Phys. Chem.* **1996**, *100*, 2001−2011. (c) Grabner, G.; Rechthaler, K.; Köhler, G. *J. Phys. Chem. A* **1998**, *102*, 689−696. (d) Baumgarten, M.; Gherghel, L.; Friedrich, J.; Jurczok, M.; Rettig, W. *J. Phys. Chem. A* **2000**, *104*, 1130−1140. (e) Inoue, Y.; Jiang, P.; Tsukada, E.; Wada, T.; Shimizu, H.; Tai, A.; Ishikawa, M. *J. Am. Chem. Soc.* **2002**, *124*, 6942−6949. (f) Keinan, S.; Hu, X.; Beratan, D. N.; Yang, W. *J. Phys. Chem. A* **2006**, *111*, 176−181. (g) Chen, Y.; Zhao, J.; Guo, H.; Xie, L. *J. Org. Chem.* **2012**, *77*, 2192−2206.

(7) (a) Shukla, D.; Wan, P. *J. Am. Chem. Soc.* **1993**, *115*, 2990−2991. (b) Yuan, C.; Saito, S.; Camacho, C.; Irle, S.; Hisaki, I.; Yamaguchi, S. *J. Am. Chem. Soc.* **2013**, *135*, 8842−8845. (c) Yuan, C.; Saito, S.; Camacho, C.; Kowalczyk, T.; Irle, S.; Yamaguchi, S. *Chem.—Eur. J.* **2014**, *20*, 2193−2200.

(8) (a) Holzapfel, M.; Lambert, C.; Selinka, C.; Stalke, D. *J. Chem. Soc., Perkin Trans. 2* **2002**, 1553−1561. (b) Miao, Q.; Nguyen, T.-Q.; Someya, T.; Blanchet, G. B.; Nuckolls, C. *J. Am. Chem. Soc.* **2003**, *125*, 10284−10287. (c) Okamoto, T.; Terada, E.; Kozaki, M.; Uchida, M.; Kikukawa, S.; Okada, K. *Org. Lett.* **2003**, *5*, 373−376. (d) Terada, E.; Okamoto, T.; Kozaki, M.; Masaki, M. E.; Shiomi, D.; Sato, K.; Takui, T.; Okada, K. *J. Org. Chem.* **2005**, *70*, 10073−10081. (e) Suzuki, S.; Takeda, T.; Kuratsu, M.; Kozaki, M.; Sato, K.; Shiomi, D.; Takui, T.; Okada, K. *Org. Lett.* **2009**, *11*, 2816−2818. (f) Wang, C.; Dong, H.; Hu, W.; Liu, Y.; Zhu, D. *Chem. Rev.* **2011**, *112*, 2208−2267. (g) Zheng, Z.; Dong, Q.; Gou, L.; Su, J.-H.; Huang, J. *J. Mater. Chem. C* **2014**, *2*, 9858−9865. (h) Huang, W.; Sun, L.; Zheng, Z.; Su, J.; Tian, H. *Chem. Commun.* **2015**, *51*, 4462−4464.

(9) (a) Hiraoka, S.; Okamoto, T.; Kozaki, M.; Shiomi, D.; Sato, K.; Takui, T.; Okada, K. *J. Am. Chem. Soc.* **2004**, *126*, 58−59. (b) Masuda, Y.; Kuratsu, M.; Suzuki, S.; Kozaki, M.; Shiomi, D.; Sato, K.; Takui, T.; Hosokoshi, Y.; Lan, X.-Z.; Miyazaki, Y. *J. Am. Chem. Soc.* **2009**, *131*, 4670−4673. (c) Masuda, Y.; Takeda, H.; Kuratsu, M.; Suzuki, S.; Kozaki, M.; Shiomi, D.; Sato, K.; Takui, T.; Okada, K. *Pure Appl. Chem.* **2010**, *82*, 1025−1032.

(10) (a) Arimori, S.; Bell, M. L.; Oh, C. S.; James, T. D. *Org. Lett.* **2002**, *4*, 4249−4251. (b) Boden, B. N.; Jardine, K. J.; Leung, A. C.; MacLachlan, M. J. *Org. Lett.* **2006**, *8*, 1855−1858. (c) Feng, X.; Pisula, W.; Müllen, K. *Pure Appl. Chem.* **2009**, *81*, 2203−2224.

(11) Morris, J.; Brühlmann, U.; Serafimov, O.; Huber, J. R. *Ber. Bunsen. Phys. Chem.* **1974**, *78*, 1348−1353.

(12) Schuster, G. B.; Schmidt, S. P.; Dixon, B. G. *J. Phys. Chem.* **1980**, *84*, 1841−1843.

(13) (a) Smith, J. G.; Levi, E. M. *J. Organomet. Chem.* **1972**, *36*, 215−226. (b) Schmidt, S. P.; Schuster, G. B. *J. Am. Chem. Soc.* **1980**, *102*, 306−314.

(14) Montalti, M.; Credi, A.; Prodi, L.; Gandolfi, M. T. *Handbook of Photochemistry*; CRC Press: Boca Raton, FL, 2006.

(15) Korppi-Tommola, J. E. I.; Hakkarainen, A.; Hukka, T.; Subbi, J. *J. Phys. Chem.* **1991**, *95*, 8482−8491.

(16) Bahri, M. A.; Heyne, B. J.; Hans, P.; Seret, A. E.; Mouithys-Mickalad, A. A.; Hoebeke, M. D. *Biophys. Chem.* **2005**, *114*, 53−61.

(17) Meijer, G.; Berden, G.; Meerts, W. L.; Hunziker, H. E.; de Vries, M. S.; Wendt, H. R. *Chem. Phys.* **1992**, *163*, 209−222.

(18) (a) Chou, P.-T.; Chen, Y.-C.; Yu, W.-S.; Chou, Y.-H.; Wei, C.-Y.; Cheng, Y.-M. *J. Phys. Chem. A* **2001**, *105*, 1731−1740. (b) Chou, P.-T.; Pu, S.-C.; Cheng, Y.-M.; Yu, W.-S.; Yu, Y.-C.; Hung, F.-T.; Hu, W.-P. *J. Phys. Chem. A* **2005**, *109*, 3777−3787.

(19) Lakowicz, J. R. *Principles of Fluorescence Spectroscopy*; Springer Science & Business Media: New York, 2007.

(20) Frisch, M. J.; et al. *Gaussian 09*, Revision A.2; Gaussian, Inc.: Wallingford, CT, 2009.